Percolation monitoring and water content estimation by Ground Penetrating Radar in a controlled environment

Matteo Dossi [a], Emanuele Forte [a,*], Sergio Andri [b], Andrea Nardini [c], Riccardo Vella [a], Michele Pipan [a]

[a] Department of Mathematics and Geosciences, University of Trieste, Via Edoardo Weiss 2, 34128 Trieste, TS, Italy
[b] Harpo S.p.A., Green Roofs Division, Research and Development Office, Via Caduti sul Lavoro 7, 34015 Muggia, TS, Italy
[c] Department of Life Sciences, University of Trieste, Via Licio Giorgieri 10, 34127 Trieste, TS, Italy

ARTICLE INFO

Article history:
Received 24 November 2020
Received in revised form 2 April 2021
Accepted 13 April 2021
Available online 17 April 2021

Keywords:
GPR
Data inversion
Water content
Water percolation
Monitoring
Green roofs

ABSTRACT

We investigated the percolation of water within a controlled environment in order to recover the EM properties and the internal structure of the materials, and to better understand the drainage processes involved. We implemented an analogue model that accurately replicates a green roof, from the construction materials to the geometry. We acquired several common offset GPR data sets on the entire surface of the model, both before and during different irrigation tests. We separately analyzed variations in the reflected amplitudes and in the EM velocities, the latter of which were calculated by combining the measured thickness of the model with the arrival times of the recorded reflections. The signal amplitudes obtained before and during irrigation are compared in order to estimate the attenuation factor at the different stages of the irrigation process. We use the attenuation factor and the EM velocities to estimate the relative permittivity of the topsoil mixture, from which we then calculate the water content, the porosity, and the relative electrical permittivity of the solid matrix by applying well known empirical formulas. The results were validated by comparing them with independent direct measurements.

1. Introduction

Ground Penetrating Radar (a.k.a. Georadar or GPR) is a non-invasive, near-surface, geophysical technique based on the propagation of EM waves in the subsurface, which are emitted and detected by antennas. By analyzing the amplitudes and travel times of the recorded signals, it is possible to obtain both qualitative and quantitative information about the materials and the structures through which the recorded signal propagated. GPR surveys have several applications in many fields, including (A) archeology, to detect buried structures and voids, and to perform pre-excavation mapping (Zhao et al., 2013); (B) engineering, for non-destructive inspections of infrastructures, and to test the integrity of construction materials (Kaur et al., 2016); (C) environment, to map and monitor the migration of pollutants within the ground, and for groundwater investigations (Jol, 2009); (D) forensic science, to locate buried targets (Almeida et al., 2014); (E) geology, to map the subsurface stratigraphy, and to detect structures such as faults, dykes, and coal seams (Ercoli et al., 2014); and (F) glaciology, to map the internal stratigraphy of glaciers and to estimate their mass balance (Dossi et al., 2018).

In this paper, we focus on an innovative environmental application, by monitoring water percolation though the topsoil of green roofs and estimating their water content, both of which are of interest in the design of irrigation and drainage processes. A green roof (a.k.a. roof garden, or vegetated-, eco-, or cool-roof) is a structure consisting of different kinds of vegetation/plants growing on topsoil contained within a waterproof system that is installed on top of a flat or slightly–sloped roof. The use of green roofs is spreading in several countries all over the world thanks to their multiple environmental, social and economic benefits (Shafique et al., 2018). In particular, several studies demonstrated that green roofs are efficient in (A) storm-water management; (B) reducing urban heat islands; (C) improving urban vegetation, wildlife habitats, and roof life; (D) enhancing the overall air and water quality; (E) decreasing the energy consumptions of buildings; (F) limiting the noise pollution; (G) offering recreational activities; and (H) increasing the green areas and aesthetic value of urban environments (Shafique et al., 2018).

Similarly to natural soils, the soil substratum of green roofs is generally made of several components, which can be mainly grouped into three distinct phases, namely a solid phase, a liquid phase, and an air phase, with porosity values mostly ranging between 20 and 40% (Jol, 2009). Pores within soils can be occupied by air, water, or pollutants (either gas or liquid) in different proportions that may change with time. In GPR applications, the electrical permittivity ε and the electrical

* Corresponding author.
E-mail address: eforte@units.it (E. Forte).

conductivity σ are the main factors governing wave propagation, while the magnetic permeability μ is rarely influential, except when a significant amount of ferromagnetic minerals is present (Jol, 2009). The penetration of GPR signals can reach hundreds of meters in low-loss materials such as ice and dry sand, while it can be limited to tens of centimeters to a few meters in highly conductive materials such as clay and sea water (Davis and Annan, 1989). The properties of the resulting soil mixture are seldom proportional to the volumetric fractions of its constituents, which makes the quantitative analysis of GPR data very difficult. Nevertheless, the presence of water dominates the EM response within the 10 MHz - 1 GHz frequency range (Jol, 2009) due to its higher polarizability ($\varepsilon_r \approx 80$) with respect to other materials, as well as its ion mobility, which increases the overall conductivity of the soil. In fact, due to the large contrast in EM properties between water and other materials, radar velocity is primarily a function of the volumetric water content when such content is higher than 5% (Topp et al., 1980). The relationship between electrical permittivity, electrical conductivity, and volumetric water content within soils has been described by several empirical models, such as the Topp relationship (Topp et al., 1980), variations of Archie's law (Archie, 1942), the Bruggeman-Hanai-Sen (BHS) model (Sen et al., 1981), the Complex Refractive Index Model (CRIM) (Wharton et al., 1980), and many others with slightly different approaches and parameters.

Extensive reviews of GPR methods for the estimation of the soil water content are given for instance in (Huisman et al., 2003; Klotzsche et al., 2018). The first paper identifies four categories of GPR methods to determine the dielectric permittivity, and consequently the soil water content, namely (A) recovery of the reflected wave velocity from single-offset and multi-offset measurements; (B) determination of the ground wave velocity; (C) recovery of the transmitted wave velocity between boreholes from zero-offset profiles and multi-offset GPR measurements; and (D) determination of the surface reflection coefficients (Huisman et al., 2003). The second paper expands on such initial categories, citing new methods of GPR data acquisition and analysis, improvements in the GPR measurement systems, and the rapid growth of computational performance, which allows the use of inversion methods that were previously not feasible (Klotzsche et al., 2018).

In this paper, we are interested in the first category of methods, namely the determination of the reflected wave velocity from Common Offset (CO) GPR data sets, whose antenna geometry is still the most commonly applied. Less widely performed types of GPR surveys encompass Multi-Offset (MO) techniques like Common Mid-Point (CMP) or Wide-Angle Reflection and Refraction (WARR) measurements, which allow the application of wave velocity analysis techniques such as reflection/diffraction hyperbola matching, normal move-out inversion, or semblance analysis (Bradford, 2006; Kaufmann et al., 2020; Diamanti et al., 2018; Angelis et al., 2019). However, MO techniques are not useful in the study of green roofs, given the low depth-to-offset ratio and the lack of large internal reflections within the topsoil. Conversely, in CO GPR data sets the subsurface velocity distribution is commonly recovered through diffraction hyperbola matching, migration velocity analysis, or amplitude inversion (Schmelzbach et al., 2012; Forte et al., 2014). Nevertheless, such techniques can also be difficult to apply in the study of green roofs, since there are usually no diffraction hyperbolas nor large internal reflections within the topsoil. Therefore, for such applications, the velocity distribution is simply derived from the measured thickness of the topsoil and the arrival times of the bottom reflection, recorded along the CO GPR data sets. A somewhat similar approach is described in (Allred et al., 2016), where the bulk volumetric water content of a sand layer across a golf green was estimated using GPR, and then validated by independent Time Domain Reflectometry (TDR) measurements.

Once we have calculated the reflected wave velocity, and therefore the relative permittivity, from the GPR data set, we can recover the soil water content by exploiting the existing empirical and physical relationships between the soil water content and the relative permittivity. The most commonly applied relationship was proposed by (Topp et al., 1980):

$$\theta = -5.3\cdot10^{-2} + 2.92\cdot10^{-2}\varepsilon_r - 5.5\cdot10^{-4}\varepsilon_r^2 + 4.3\cdot10^{-6}\varepsilon_r^3 \quad (1)$$

where θ is the volumetric soil water content and ε_r is the relative electrical permittivity (a.k.a. dielectric constant). Appropriate for the typical frequency range of GPR (10 MHz - 1 GHz), this equation agrees reasonably well with the experimental results across a wide range of water contents (~5–50%), however for more accurate results it requires the selection of appropriate coefficients from the experimental data (Jol, 2009).

A simple linear relationship between the complex refractive index, which is similar to $\sqrt{\varepsilon_r}$, and the volumetric water content θ, was also showed in (Topp et al., 1980). The generalized empirical equation proposed by manufacturers for mineral soils (i.e. generic soils with low organic matter) is given by (Di Matteo et al., 2018):

$$\sqrt{\varepsilon_r} = 1.6 + 8.4\theta \quad (2)$$

Nevertheless, the coefficients of this formula also require appropriate calibration for specific types of soils (Di Matteo et al., 2018). Another widely accepted, more general formula is given by (Annan, 1999):

$$\varepsilon_r = 3.03 + 9.3\theta + 146\theta^2 - 76.6\theta^3 \quad (3)$$

However, this equation is no longer applicable in the case of clayed and organic soils, since the material is assumed to be low-loss and having a dry state relative permittivity around 3–4.

A more theoretical relationship is given by dielectric mixing models, such as the CRIM model, which uses the volumetric fractions and the relative permittivities of the three main constituents of the soil (i.e. solid, water, and air), and is given by the following equation (Birchak et al., 1974):

$$\varepsilon_r = (\theta\sqrt{\varepsilon_{r,w}} + (1-\phi)\sqrt{\varepsilon_{r,s}} + (\phi-\theta)\sqrt{\varepsilon_{r,a}})^2 \quad (4)$$

where ϕ is the porosity.

By rearranging this equation, we obtain the following relationship between the soil water content θ and the relative permittivity ε_r, which recalls the linear relationship from Eq. (2):

$$\theta = \frac{\sqrt{\varepsilon_r}}{(\sqrt{\varepsilon_{r,w}}-1)} + \frac{(\phi-1)\sqrt{\varepsilon_{r,s}}-\phi}{(\sqrt{\varepsilon_{r,w}}-1)} \quad (5)$$

with

$$\varepsilon_{r,a} = 1 \quad (6)$$

In order to use the CRIM equation, we must be able to recover the porosity ϕ of the analyzed material and there are several possible methods to achieve this. It is important to point out that the effective porosity is limited to the connected pores, which allow fluids to flow within the soil, while the total porosity also comprises unconnected pores, as well as the space occupied by immobile water in clays 25]. A simple method to calculate the effective porosity is to measure the displacement within a water-filled tank after submerging dried soil samples and applying constant vacuum to eliminate bubbles (Conti et al., 2019). Another technique integrates GPR attributes in order to calculate the porosity from core samples, for example by using shadow zones within the instantaneous amplitude and the instantaneous frequency profiles to highlight higher secondary porosity zones in karstified carbonate rocks (Conti et al., 2019). A third method uses a simplified version of the CRIM equation, considering fully saturated models, where the volumetric water content is considered equal to the porosity, while disregarding the adsorbed water (Causse and Sénéchal, 2006;

Bradford et al., 2009). In this paper, we also exploit fully saturated conditions, as well as dry and partially saturated conditions, and by repeating the GPR measurements during the irrigation process, we can monitor the evolution of the water content and estimate the porosity of the analyzed topsoil model.

2. Experimental setting

We constructed a model that reproduces a portion of a green roof, maintaining the structural geometry and using the same construction materials, but we did not include living plants, roots, or any other organic matter, thus replicating the structure soon after emplacement. The model is placed within a semi-transparent plastic container in order to limit border effects during the GPR data acquisition and to make the water percolation and drainage observable from the outside in real time. The plastic container narrows at the base, being 72 × 50 cm in size at the top and 65 × 45 cm in size at the bottom. The model structure and filling materials, provided by Harpo S.p.A., include from top to bottom: a 11 cm thick soil layer; a 0.5 mm thick filtering towel; 4 cm deep bowls for water drainage; a 5–10 mm thick Harpo® retainer filter; a few mm thick impermeable anti-root membrane; a basal aluminum sheet used as reference for GPR signals; and the bottom of the plastic container. On one side of the box two drains were fixed in order to carry off excess water from the basal bowls (Fig. 1).

The soil layer is made of technogenic topsoil with known chemical and physical properties (data from http://www.harpogroup.it/verdepensile - in Italian), 80% of which consists of porous mineral materials, with a negligible content of water (during preparation). The maximum compaction reaches 20%, while the hydraulic conductivity is as high as 20 mm/min (DIN 18035). The apparent density is within the 850–1000 kg/m^3 range (UNI EN 13041), the electrical conductivity is in the 5–25 mS/m range (UNI EN 13038), the pH is between 6 and 7.8, and the cation exchange capacity is between 15 and 25 meq/100 g (DM 11/05/92 met. 27). The artificial topsoil has a content of less than 3% for particles having a grain size smaller than 0.05 mm, less than 5% (in mass) for organic matter, and does not contain toxic materials or infesting plants seeds.

We performed the GPR measurements, both before and during irrigation, using a ProEx GPR system equipped with 2.3 GHz ground-coupled bistatic Malå Geoscience shielded antennas, with a constant transmitter-receiver offset equal to 4 cm. The data acquisition grid used before irrigation included 8 longitudinal and 8 transversal GPR profiles, with a space interval between them equal to 4.5 cm (Fig. 2). During the irrigation process, we regularly repeated the 8 longitudinal profiles, as well as 3 additional acquisitions along profile P4 (Fig. 2). In particular, the irrigation process consisted in pouring several volumes of water, respectively equal to 1, 2, 3, and 6 liters, over half of the topsoil surface, at time intervals equal to approximately 20 min each. During such intervals we performed GPR measurements along the 11

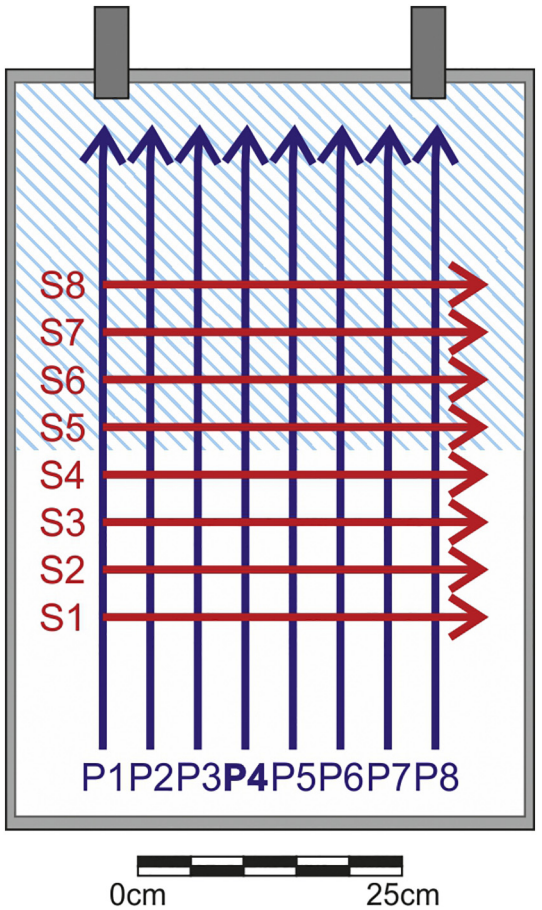

Fig. 2. Spatial positions of the GPR profiles recorded over the topsoil surface within the plastic container. The measurements were performed along all profiles in dry conditions and then repeated along just the longitudinal profiles (Pn) during the irrigation process. Furthermore, profile P4 was acquired more than once between irrigation steps, respectively 3, 7, 10, and 15 min after each pouring, while profiles P4 and P5 were also repeated in fully saturated conditions. The light blue pattern represents the irrigated area of the model. (For interpretation of the references to colour in this figure legend, the reader is referred to the web version of this article.)

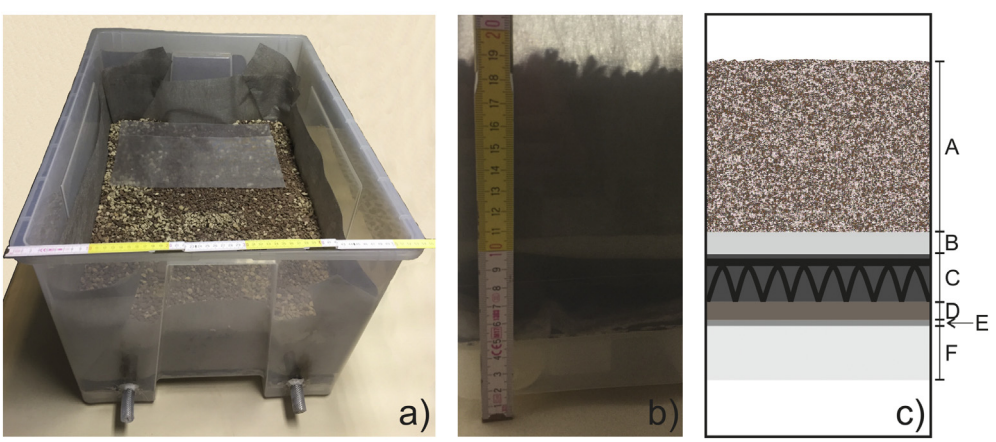

Fig. 1. Pictures of the green roof model placed within its plastic container, which is used for the controlled experiment (a; b), and the outline of the structure and materials used (c), which include: A) a soil layer (substratum); B) a filtering towel; C) plastic bowls; D) a retainer filter; E) an anti root membrane and an aluminum sheet; and F) the bottom of the plastic container. (For interpretation of the references to colour in this figure legend, the reader is referred to the web version of this article.)

aforementioned longitudinal profiles, in order to observe the effects of water percolation on the EM response of the topsoil.

Although water started to flow from the drains after the last 6 l were poured, initially suggesting that the topsoil was fully (or almost fully) saturated, preliminary results from the recorded amplitudes indicated that this was not probably the case, since the calculated porosity values were significantly lower than the ones obtained from independent direct measurements. Therefore, in order to make sure that the topsoil was actually fully saturated, the experiment was repeated after placing the plastic container inside a larger plastic tub, which was then filled with water up to the topsoil surface, allowing water penetration from the bottom through the two basal drains. The GPR measurements were then repeated along profiles P4 and P5, with the calculated porosity reaching values consistent with the independent direct measurements.

We analyzed the peak amplitudes and arrival times of the basal topsoil reflection in the recorded longitudinal profiles, by applying an automated picking procedure (Dossi et al., 2015a; Dossi et al., 2015b; Forte et al., 2016) to each data set, thus ensuring the accurate sampling of the peak amplitudes in all the GPR traces (Fig. 3). The reflected amplitudes obtained after each irrigation step are plotted in Fig. 4, and they clearly show the water propagation from one end of the container to the other, based on the amplitude decay measured in different positions and at different stages.

3. Theory and methods

Several factors can reduce the amplitude of GPR waves during propagation, including: (A) intrinsic attenuation, which is associated with energy loss due to electric currents (conductivity) and molecular polarization (dielectric relaxation) caused by the changing electric field; (B) wavefront expansion, which involves the spreading of the energy initially emitted by the antenna over an ever-increasing surface; (C) scattering, which is caused by the interaction of the EM signals with soil particles (e.g. granules within sediments, crystals within rocks, or voids within both) having dimensions comparable with the wavelength, resulting in the EM signal being re-emitted in all directions; (D) partial reflections, which involve the partitioning of the signal energy at various interfaces with different EM impedance contrasts.

Considering a single-frequency, linearly polarized, EM plane wave propagating through a homogeneous material and reflected by a single interface, its propagation is described by the following equation for the electric field:

$$E(r,t) = \frac{E_0 R}{1+r} e^{\alpha r} e^{i(\beta r - \omega t)} \tag{7}$$

with

$$\alpha = \alpha_o + \alpha_s \tag{8}$$

$$v = \frac{\omega}{\beta} \tag{9}$$

where E_0 is the initial amplitude of the emitted signal, R is the reflection coefficient at the interface, the $\frac{1}{1+r}$ factor describes wavefront expansion, r is the travelled distance, v is the propagation velocity, ω is the angular frequency, β is the wavenumber, i is the imaginary unit, and α is the attenuation factor, made of a conductive part α_o and a scattering part α_s.

In the case of our model, the reflection interface is between the topsoil and an air layer made up of the water drainage plastic bowls, therefore the signal velocities in the two layers are given by:

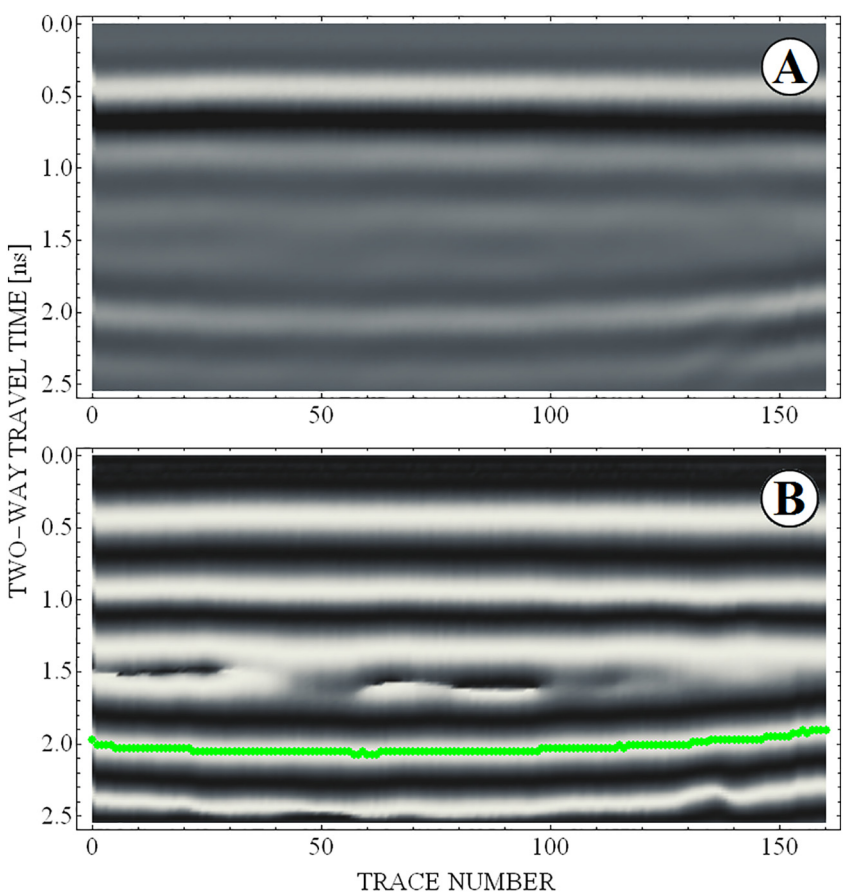

Fig. 3. Example of automated picking applied to one of the GPR profiles acquired over the topsoil model in dry conditions. The figure shows the amplitude profile (A), as well as the corresponding cosine phase profile (B). The horizon marking the main phase of the reflection from the bottom of the topsoil is superimposed in (B).

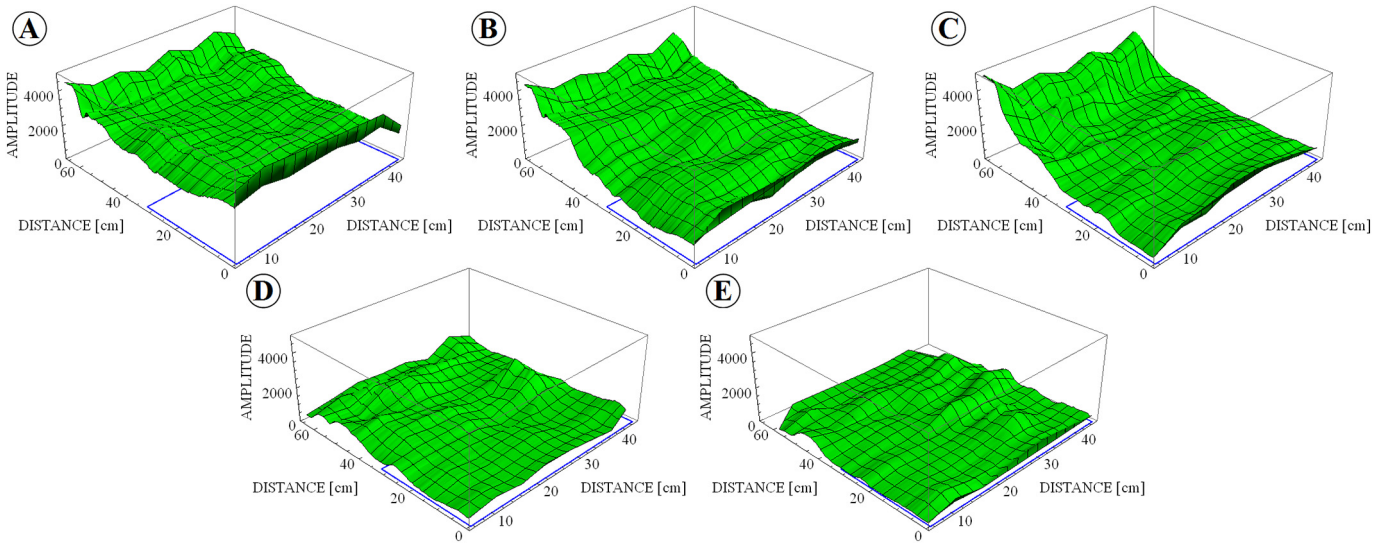

Fig. 4. Amplitudes of the GPR signals reflected from the bottom of the topsoil, shown at different stages of the irrigation process, namely the dry case (A), and after 1 (B), 3 (C), 6 (D), and 12 (E) liters of poured water. The blue rectangles highlight the irrigated half of the model. We can easily notice the water propagation from one end of the plastic container to the other, based on the decrement of the reflection amplitudes from (A) to (E). (For interpretation of the references to colour in this figure legend, the reader is referred to the web version of this article.)

$$v_1 = \frac{2\sqrt{\left(\frac{x}{2}\right)^2 + H^2}}{TWT} \tag{10}$$

$$v_2 \approx c \tag{11}$$

where x is the transmitter-receiver offset, H is the thickness of the topsoil layer, TWT is the two-way traveltime of the recorded signal, and c is the radar velocity in air (i.e. about 30 cm/ns). In the fully saturated conditions, when the model is placed within a water-filled tub, the air within the drainage bowls is completely replaced by water, therefore the EM velocity v_2 within the second layer becomes equal to 3.3 cm/ns (Davis and Annan, 1989).

From the velocities v_1 and v_2, we are able to recover the reflection coefficient at the bottom topsoil-air interface using the following Fresnel equation:

$$R = \frac{\sin\left[\theta_t - \theta_i\right]}{\sin\left[\theta_t + \theta_i\right]} \tag{12}$$

with

$$\theta_i = \tan^{-1}\left[\frac{x}{2H}\right] \tag{13}$$

$$\theta_t = \sin^{-1}\left[\frac{v_2}{v_1}\sin\theta_i\right] \tag{14}$$

where θ_i and θ_t are the incidence and transmission angles, respectively.

Considering the topsoil model and two signals recorded in the same position at different irrigation times, the recorded peak amplitudes are given by the following equations:

$$A_1 = \frac{A_0 R_1}{1+r} e^{\alpha_1 r} \tag{15}$$

$$A_2 = \frac{A_0 R_2}{1+r} e^{\alpha_2 r} \tag{16}$$

with

$$r = 2\sqrt{\left(\frac{x}{2}\right)^2 + H^2} \tag{17}$$

By dividing the two recorded peak amplitudes A_1 and A_2, it is possible to isolate the difference in the attenuation factors:

$$\alpha_1 - \alpha_2 = -\frac{\ln\left[\frac{A_1 R_2}{A_2 R_1}\right]}{r} \tag{18}$$

If we assume that the peak amplitude A_1 is recorded in absence of any intrinsic or scattering attenuation, which in this case would be before the irrigation process, when the water content is negligible, then the attenuation factor for the peak amplitude A_2 is given by the following equation:

$$\alpha_2 = \frac{\ln\left[\frac{A_1 R_2}{A_2 R_1}\right]}{r} \tag{19}$$

with

$$\alpha_1 \approx 0 \tag{20}$$

We can disregard the scattering attenuation, this being a realistic assumption when grain dimensions are smaller than the dominant wavelength, and thus we can approximate the attenuation factor with just the intrinsic attenuation. In fact, considering for example a 2.3 GHz single-frequency EM wave propagating though a homogeneous medium with a velocity of 10 cm/ns, the corresponding wavelength is equal to 4.3 cm, which is about one order of magnitude larger than the average grain size for the analyzed model. Under these conditions, we can use the following equations to describe the wave propagation (Jol, 2009):

$$\alpha = \omega\sqrt{\frac{\mu\varepsilon}{2}\left[\sqrt{1+\left(\frac{\sigma}{\omega\varepsilon}\right)^2} - 1\right]} \tag{21}$$

$$v = \frac{c}{\sqrt{\frac{\mu_r\varepsilon_r}{2}\left[\sqrt{1+\left(\frac{\sigma}{\omega\varepsilon}\right)^2} + 1\right]}} \tag{22}$$

These two equations can be combined in order to obtain the formulas for the relative electrical permittivity ε_r and the electrical conductivity σ:

$$\varepsilon_r = \frac{\omega^2 - \alpha^2 v^2}{\mu_0 \varepsilon_0 v^2 \omega^2} \tag{23}$$

$$\sigma = \frac{2\alpha}{\mu_0 v} \tag{24}$$

with

$$\varepsilon = \varepsilon_0 \varepsilon_r \tag{25}$$

$$\mu = \mu_0 \tag{26}$$

where the relative magnetic permeability μ_r is considered equal to 1 for non-ferromagnetic materials. If we set the attenuation factor α equal to 0, the permittivity and conductivity equations are further simplified as:

$$\varepsilon_r = \left(\frac{c}{v}\right)^2 \tag{27}$$

$$\sigma = 0 \tag{28}$$

with

$$c = \frac{1}{\sqrt{\mu_0 \varepsilon_0}} \tag{29}$$

4. Results and discussion

In this section, we mostly discuss the results obtained from profile P4, for which we have the largest number of data sets (i.e. 18 recordings in total). The results from this profile can be considered representative of the results obtained from the whole model, given the repetitiveness of the GPR system. In fact, Fig. 5 highlights this repetitiveness, showing negligible changes in the average reflection amplitudes, except for limited border effects. The GPR traces were not acquired with a numerically controlled positioning system (e.g. (Delgado et al., 2019)) and the match between trace locations in different profiles is not perfect. We therefore used as input amplitudes in Eq. (19) the average values of the amplitudes recorded in the irrigated half of the model (Fig. 2), in both the dry and wet conditions. We then calculated the relative permittivity (Eq. (23)) and the electrical conductivity (Eq. (24)), and the results are shown in Table 1, with both values significantly increasing with wetness, as expected. Moreover, if we use the relative permittivity estimated in the fully saturated case in the Topp equation (Eq. (1)), we obtain a water content equal to 32.6% for profile P4, and 34.4% for profile P5. Both values are consistent with independent direct measurements, which give a value equal to 33.4% for the water content, and they can also be considered estimates of the porosity of the saturated topsoil, assuming that the GPR profiles acquired before the irrigation process were made in perfectly dry conditions. More specifically, we estimated the volume of each part of the model (i.e. the topsoil, the plastic bowls, and the retainer filter, while the volume of the filtering towel was considered negligible). We then compared the reference values for water retention given by Harpo S.p.A. in the saturated conditions (i.e. 4 L/m^3 for the topsoil, 4 L/m^3 for the water drainage bowls, and 2 L/m^3 for the retainer filter) with the direct measurements of the total amount of water needed to saturate the model. For this latter estimate, we measured the weight of the model, including its plastic container, both before the irrigation process and after its saturation by immersion in a water-filled tub. As previously discussed, the results from the GPR profiles are in quite good agreement with the direct measurements. This is an important result, since we were able to recover the porosity of the topsoil by performing just two GPR measurements, in dry and saturated conditions, respectively.

If we combine the estimated value of the porosity with the CRIM (Eq. (4)) and Topp (Eq. (1)) equations, we can calculate the relative permittivity of the solid matrix of the topsoil using the following equation, obtained by rearranging the CRIM equation:

$$\varepsilon_{r,s} = \left(\frac{\sqrt{\varepsilon_r} + (\theta - \phi)\sqrt{\varepsilon_{r,a}} - \theta\sqrt{\varepsilon_{r,w}}}{1 - \phi}\right)^2 \tag{30}$$

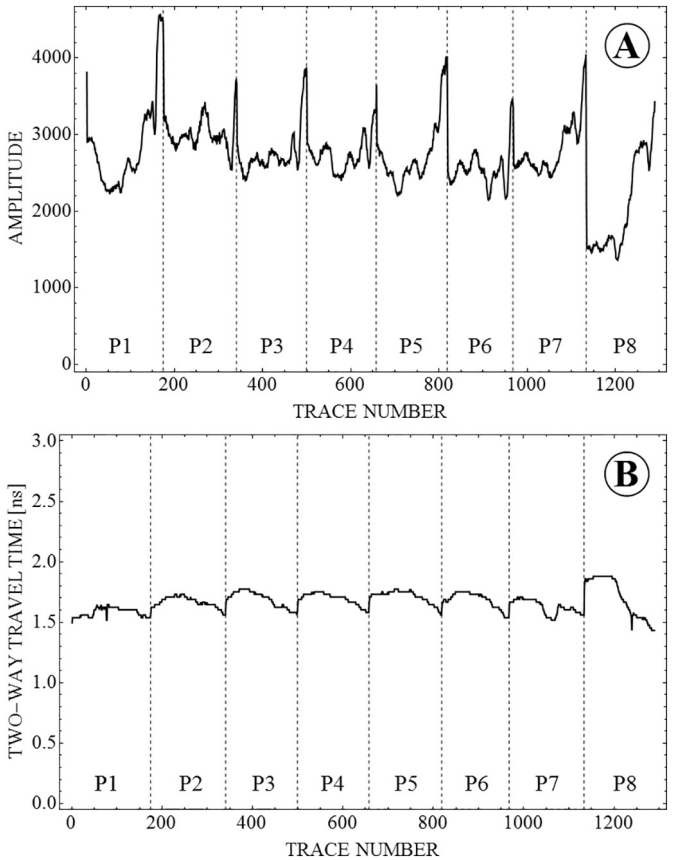

Fig. 5. Recorded reflection amplitudes (A) and travel times (B) along the 8 longitudinal GPR profiles acquired over the topsoil in dry conditions. The graphs show fairly repetitive data, except for some border effects at the ends of each profile, especially in the profiles acquired near the borders of the plastic container (i.e. P1 and P8). The travel times in (B) show a moderate increase towards the center of the container, indicating a deformation of its plastic bottom, which was caused by the weight of the topsoil.

The results are shown in Table 1, with a mean value of $\varepsilon_{r,s}$ equal to 3.97 and a slight increase in the estimated value with wetness, while for comparison the relative permittivity of the mixture in the dry case (Eqs. (10) and (27)) is 5.37.

Another way to calculate $\varepsilon_{r,s}$ is to fit Eq. (5) to the graph of the soil water content as a function of the square root relative permittivity, as shown in Fig. 6, which selectively analyzes the four central GPR profiles (i.e. profiles 3, 4, 5, and 6) in order to avoid border effect from the plastic container (Fig. 2). The resulting permittivities of the solid matrix $\varepsilon_{r,s}$ are very similar, being respectively equal to 2.57, 3.06, 3.15, and 2.45, but they are significantly different from the value of 3.97 calculated earlier. In fact, these results strongly depend on the Topp equation (Eq. (1)), which is used to calculate the water content from the permittivities, and thus leads to the highlighted linear trends (Eq. (2)).

The proposed method is quite robust, since the estimates obtained for the same irrigation step at different times are in fact coherent, with the exception of a few outliers. In particular, a significant increase of the electrical conductivity for increasing water contents is apparent, while the corresponding increase of the electrical permittivity is relatively smaller (Table 1). This behavior could be related to the water relaxation process, which at frequencies higher than about 1GHz causes

Table 1
Calculated values for the relative permittivity ε_r, the electrical conductivity σ, and the relative permittivity of the solid matrix $\varepsilon_{r,s}$, the latter being estimated using a porosity of 34.4% in Eq. (30).

Water poured [L]	Elapsed time [min]	ε_r (Eq. (23))	σ [mS/m] (Eq. (24))	$\varepsilon_{r,s}$ (Eq. (30))	Water poured [L]	Elapsed time [min]	ε_r (Eq. (23))	σ [mS/m] (Eq. (24))	$\varepsilon_{r,s}$ (Eq. (30))
1	3	5.37	39.7	3.74	**6**	3	7.77	118.4	3.99
	7	5.57	37.4	3.78		7	9.50	126.6	4.05
	10	5.53	35.2	3.77		10	8.86	121.5	4.03
	15	5.54	35.1	3.77		15	8.96	122.6	4.04
3	3	5.51	51.9	3.77	**12**	3	8.85	167.2	4.03
	7	7.95	74.0	4.00		7	10.16	237.5	4.07
	10	7.81	70.8	3.99		10	9.58	247.2	4.05
	15	7.82	73.6	3.99		15	10.68	291.1	4.08
					Full		18.52	462.3	4.34

The parameters were obtained from the reflected amplitudes and travel times recorded along profile 4 for increasing times (i.e. 3, 7, 10 and 15 min) after each irrigation step. The last parameters where obtained in the fully saturated conditions.

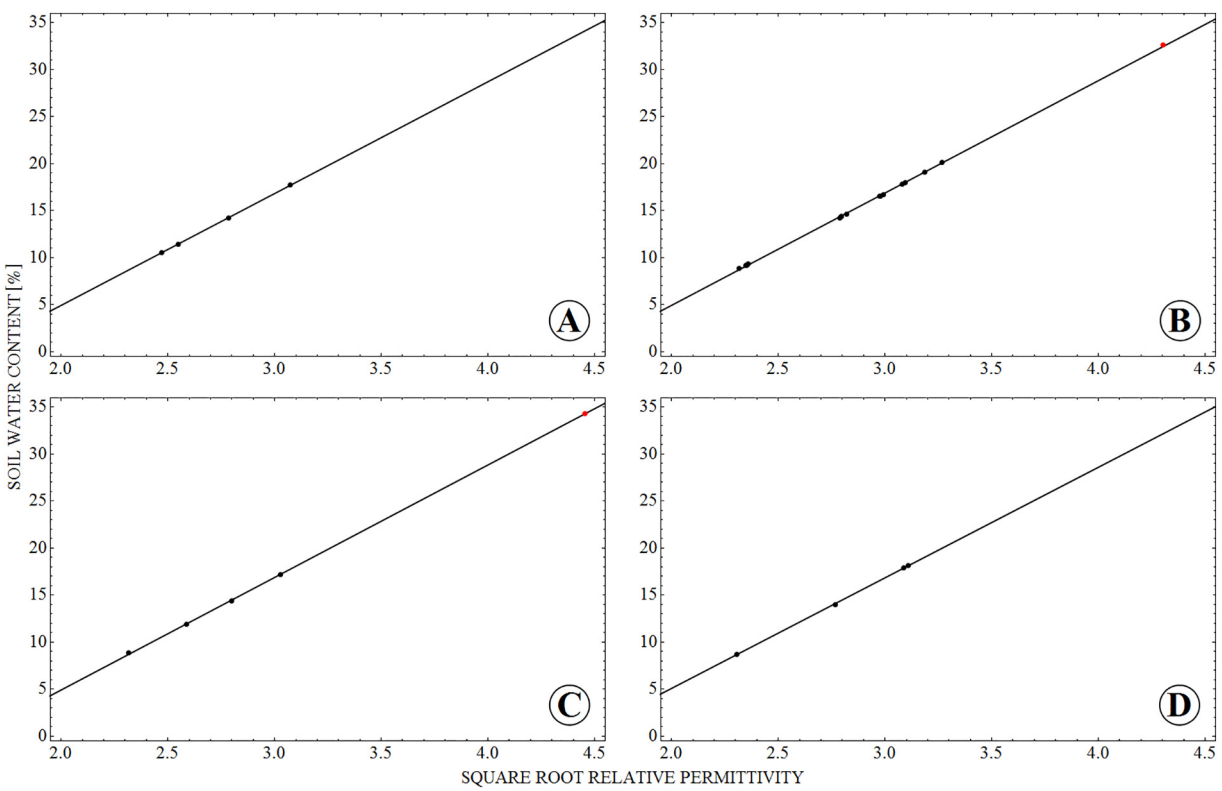

Fig. 6. Graphs of the soil water content plotted as a function of the square root relative permittivity, as calculated from the profiles P3 (A), P4 (B), P5 (C), and P6 (D), which were specifically selected in order to avoid border effects from the plastic container. The red dots in (B) and (C) were calculated in the fully saturated conditions. Notice that profile P4 (B) has many more data points, due to the larger number of repeated GPR measurements (i.e. 18 in total). (For interpretation of the references to colour in this figure legend, the reader is referred to the web version of this article.)

remarkable energy dissipation due to the increase of the overall electrical conductivity (Annan, 2005). However, the correlation between the electrical permittivity and the water content is also apparent and it only shows a limited dependence on the position of the collected GPR profiles. With the exception of some border effects, all the profiles lead to very similar and consistent results at each irrigation step. Furthermore, the estimated water contents are consistent and comparable with the values independently obtained using the parameters, which were measured in laboratory by Harpo S.p.A.. However, in order to infer realistic porosity values, it is essential to ensure that the analyzed topsoil actually is in dry and saturated conditions, before comparing the respective reflected amplitudes.

5. Conclusion

We constructed a model of a green roof and studied its behavior at different stages of irrigation using GPR, in order to recover its EM properties, as well as its internal structure. The irrigation was limited to half of the model, and the water diffusion to the other half was clearly identified in the GPR profiles through the resulting amplitude attenuation. From the attenuation factor, we then obtained the relative permittivity of the topsoil mixture, its water content, its porosity, and the relative permittivity of the solid matrix. All such information can be used to better understand irrigation and drainage processes within green roofs. In particular, non-destructive measurements of the aforementioned

properties might be very useful to assess the long-term changes in the performance of the technological substrates used for green roofs, which can be affected by environmental and biological agents operating in such artificial ecosystems. GPR survey of green roofs might also help in optimizing the irrigation strategies, which are the key for implementing green roof technologies in arid-prone habitats, while also ensuring a sustainable use of irrigation water. Furthermore, the measurements and calculations reported in this study might be very useful in other contexts, such as natural or agricultural ecosystems characterized by a shallow topsoil above the underlying bedrock, which represent a challenging environment for vegetation growth and are prone to a decline in productivity and vegetation cover, especially due to droughts connected with the global climate change. Non-destructive and highly repeatable (both in space and time) measurements of water infiltration rates, water content, and related physical parameters would potentially provide important information on the vulnerability of such natural systems with respect to the changing climate.

Author contributions

EF conceived the study and designed the experiments together with SA and MD. RV built the testing model. EF, MD, and RV performed the controlled measurements and the GPR data analysis. SA, MD, EF, AN, and MP critically discussed the experimental results implementing the new experimental settings. MD and EF wrote the manuscript with the contribution of all co-authors.

Declaration of Competing Interest

The authors declare that they have no known competing financial interests or personal relationships that could have appeared to influence the work reported in this paper.

Acknowledgments

We gratefully acknowledge Harpo S.p.A. for the materials provided, as well as their technical support during the implementation of the experiment, and the Matlab campus grant for the University of Trieste. Two anonymous reviewers are acknowledge for their suggestions and comments.

References

Allred, B., Freeland, R., Grote, K., McCoy, E., Martinez, L., Gamble, D., 2016. Ground-penetrating radar water content mapping of golf course green sand layers. J. Environ. Eng. Geophys. 21 (4), 215–229.

Almeida, E.R., Porsani, J.L., Catapano, I., Gennarelli, G., Soldovieri, F., 2014. GPR data analysis enhanced by microwave tomography for forensic archaeology. Proc. IEEE 15th International Conference on Ground Penetrating Radar (GPR 2014), Brussels, Belgium, pp. 493–497 June 30–July 4.

Angelis, D., Warren, C., Diamanti, N., 2019. Preliminary development of a workflow for processing multi-concurrent receiver GPR data. Proc. 10th International Workshop on Advanced Ground Penetrating Radar (IWAGPR 2019), The Hague, Netherlands, pp. 1–7 September 8-12.

Annan, A.P., June 1999. Ground Penetrating Radar: Workshop Notes. Sensors and Software Inc., Ontario, Canada.

Annan, A.P., 2005. Ground-penetrating radar, in near-surface geophysics. In: Butler, D.K. (Ed.), Society of Exploration Geophysicists. 13. Society of Exploration Geophysicists, Tulsa, Oklahoma, pp. 357–438.

Archie, G.E., 1942. The electrical resistivity log as an aid in determining some reservoir characteristics. Trans. AIME 146, 54–62.

Birchak, J.R., Gardner, C.G., Hipp, J.E., Victor, J.M., 1974. High dielectric constant microwave probes for sensing soil moisture. Proc. IEEE 62 (1), 93–98.

Bradford, J.H., 2006. Applying reflection tomography in the postmigration domain to multifold ground-penetrating radar data. Geophysics 71 (1), K1–K8.

Bradford, J.H., Clement, W.P., Barrash, W., 2009. Estimating porosity with ground-penetrating radar reflection tomography: A controlled 3-D experiment at the Boise Hydrogeophysical Research Site. Water Resour. Res. 45 (4) (W00D26).

Causse, E., Sénéchal, P., 2006. Model-based automatic dense velocity analysis of GPR field data for the estimation of soil properties. J. Geophys. Eng. 3 (2), 169–176.

Conti, I.M.M., de Castro, D.L., Bezerra, F.H.R., Cazarin, C.L., 2019. Porosity estimation and geometric characterization of fractured and karstified carbonate rocks using GPR data in the Salitre Formation, Brazil. Pure Appl. Geophys. 176, 1673–1689.

Davis, J.L., Annan, A.P., 1989. Ground-Penetrating Radar for high resolution mapping of soil and rock stratigraphy. Geophys. Prospect. 37 (5), 531–551.

Delgado, A., Novo, A., Hays, D.B., 2019. Data acquisition methodologies utilizing ground penetrating radar for Cassava (Manihot Esculenta Crantz) root architecture. Geosciences 9, 171–183.

Di Matteo, L., Pauselli, C., Valigi, D., Ercoli, M., Rossi, M., Guerra, G., Cambi, C., Ricco, R., Vinti, G., 2018. Reliability of water content estimation by profile probe and its effect on slope stability. Landslides 15, 173–180.

Diamanti, N., Elliott, J., Jackson, R., Annan, A.P., 2018. The WARR machine: System design, implementation and data. J. Environ. Eng. Geophys. 23, 469–487.

Dossi, M., Forte, E., Pipan, M., 2015a. Automated reflection picking and polarity assessment through attribute analysis: Theory and application to synthetic and real ground-penetrating radar data. Geophysics 80 (5), H23–H35.

Dossi, M., Forte, E., Pipan, M., 2015b. Auto-picking and phase assessment by means of attribute analysis applied to GPR pavement inspection. Proc. IEEE 8th International Workshop on Advanced Ground Penetrating Radar (IWAGPR 2015), Florence, Italy, pp. 1–4 July 7-10.

Dossi, M., Forte, E., Pipan, M., Colucci, R.R., 2018. Quantitative 3-D GPR analysis to estimate the total volume and water content of a glacier. Proc. IEEE 17th International Conference on Ground Penetrating Radar (GPR 2018), Rapperswil, Switzerland, pp. 1–6 June 18-21.

Ercoli, M., Pauselli, C., Frigeri, A., Forte, E., Federico, C., 2014. 3-D GPR data analysis for high resolution imaging of shallow subsurface faults: the Mt. Vettore case study (Central Apennines, Italy). Geophys. J. Int. 198 (1), 609–621.

Forte, E., Dossi, M., Pipan, M., Colucci, R.R., 2014. Velocity analysis from common offset GPR data inversion: Theory and application to synthetic and real data. Geophys. J. Int. 197 (3), 1471–1483.

Forte, E., Dossi, M., Pipan, M., Del Ben, A., 2016. Automated phase attribute-based picking applied to reflection seismics. Geophysics 81 (2), V141–V150.

Huisman, J.A., Hubbard, S.S., Redman, J.D., Annan, A.P., 2003. Measuring soil water content with ground penetrating radar: a review. Vadose Zone J. 2, 476–491.

Jol, H.M., 2009. Ground Penetrating Radar: Theory and Applications. Elsevier Science Ltd. (524 pp).

Kaufmann, M.S., Klotzsche, A., Vereecken, H., van der Kruk, J., 2020. Simultaneous multi-channel multi-offset ground-penetrating radar measurements for soil characterization. Vadose Zone J. 19 (1), 1–18.

Kaur, P., Dana, K.J., Romero, F.A., Gucunski, N., 2016. Automated GPR rebar analysis for robotic bridge deck evaluation. IEEE Trans. Cybern. 46 (10), 2265–2276.

Klotzsche, A., Jonard, F., Looms, M.C., van der Kruk, J., Huisman, J.A., 2018. Measuring soil water content with ground penetrating radar: a decade of progress. Vadose Zone J. 17 (1), 1–9.

Schmelzbach, C., Tronicke, J., Dietrich, P., 2012. High-resolution water content estimation from surface-based ground-penetrating radar reflection data by impedance inversion. Water Resour. Res. 48 (8), 1–16.

Sen, P.N., Scala, C., Cohen, M.H., 1981. A self-similar model for sedimentary rocks with application to the dielectric constant of fused glass beads. Geophysics 46, 781–795.

Shafique, M., Kim, R., Rafiq, M., 2018. Green roof benefits, opportunities and challenges - a review. Renew. Sust. Energ. Rev. 90, 757–773.

Topp, G.C., Davis, J.L., Annan, A.P., 1980. Electromagnetic determination of soil water content: Measurements in coaxial transmission lines. Water Resour. Res. 16 (3), 574–582.

Wharton, R.P., Hazen, G.A., Rau, R.N., Best, D.L., 1980. Electromagnetic propagation logging: Advances in technique and interpretation. Soc. Petr. Eng., AIME, Paper. 9267.

Zhao, W., Forte, E., Pipan, M., Tian, G., 2013. Ground Penetrating Radar (GPR) attribute analysis for archaeological prospection. J. Appl. Geophys. 97, 107–117.